Water droplet erosion behaviour of gas nitrided Ti6Al4V

M.S. Mahdipoor [a], D. Kevorkov [a], P. Jedrzejowski [b], M. Medraj [a,c]

[a] Department of Mechanical and Industrial Engineering, Concordia University, 1455 de Maisonneuve Boulevard West, QC, Montreal, Canada H3G 1M8
[b] Siemens Canada Ltd. Energy, 9545 Cote-de-Liesse, Dorval, QC, Canada H9P 1A5
[c] Department of Mechanical and Materials Engineering, Masdar Institute, Masdar City, Abu Dhabi, UAE, P.O. Box 54224

ABSTRACT

Ti6Al4V is one of the most commonly used materials for turbine blades and improving its water erosion resistance, a typical reason for the blades' failure, is of great interest. In this work gas nitriding was applied on Ti6Al4V and its influence on water droplet erosion performance was investigated. Nitriding was carried out at 1173 and 1323 K temperatures using two different nitriding atmospheres, N_2 and N_2–4%H_2 for 5 and 10 h. The microstructure of specimens was investigated using optical microscope (OM) and scanning electron microscope (SEM). The phases formed after nitriding treatments were analysed using X-ray Diffraction (XRD). Vickers indenter was used to carry out the surface and profile microhardness measurements. The erosion tests were performed using 464 μm droplets impacting the samples at 300 and 350 m/s speeds. The nitrided specimens at 1173 K, which is below β-transus temperature of Ti6Al4V, displayed the best erosion resistance measured by their corresponding cumulative material loss, about two times higher than non-treated Ti6Al4V. The long exposure to nitriding was not beneficial for the erosion performance. The specimen nitrided in the N_2–4%H_2 atmosphere showed slightly higher resistance to erosion than those nitrided in N_2 atmosphere. The latter is due to the formation of a hard and dense compound layer that was deposited due, in part, to the presence of the reducing environment.

© 2016 Elsevier B.V. All rights reserved.

1. Introduction and literature review

Titanium alloys and mostly Ti6Al4V, which has high specific in particular strength and toughness, display superior mechanical properties and corrosion resistance. They are extensively being used in aerospace, aviation, and marine industries [1,2]. However, they suffer from some mechanical degradations in service conditions such as water droplet erosion, observed on the leading edges of turbine blades [3]. When inlet air cooling system for the gas turbine is in use, the compressors' blades are slowly eroded by the water droplet impingements [3,4]. Few studies have been performed to explore the WDE mechanisms of Ti6Al4V, and surface and sub-surface cracking were highlighted as the main contributors for the erosion damage [5–7]. WDE initiation is mostly associated with the grain boundaries damage [5], whilst in the later stages the erosion damage is predominantly governed by transgranular cracking [6,7].

Water droplet erosion is a progressive mechanical damage and a combination of several phenomena. It is caused by successive high speed impacts of small water droplets on a solid surface [3,8]. The water hammering, stress wave generation, radial outflow jetting and hydraulic (water) penetration were usually described as the most destructive phenomena during the water droplet erosion [3,9]. Increasing the hardness, while keeping the homogeneous microstructure on the surface, was found to be a promising approach to combat these destructive phenomena and improve erosion performances [3,8,10–13]. High tendency of titanium for chemical reactions at high temperatures provides large possibility of diffusion-based treatments to increase surface hardness [10,14]. Nitriding treatments (gas, plasma, and laser based) have been applied to increase the surface hardness and their influence was studied on wear, fatigue and cavitation erosion behaviors of titanium alloys [12,15–20]. However, it has rarely been investigated for water droplet erosion [12].

Gas nitriding is a practical and applicable technique to strengthen the surface of titanium alloys. The high solubility of nitrogen in α-titanium and its diffusion into this metal (activated by high temperature) results in hardening of the surface [21–23]. It is a cost-effective technique that is not sensitive to the specimen's geometry [10,21]. However, the high temperature required for gas nitriding (more than 1023 K) can be a major drawback, since it may influence the microstructure and properties of the core material [14,22,24]. Nevertheless, if this process is applied using heating techniques that generate localized heating at the surface, the impact on bulk microstructures can be minimized. Cross sectional microstructure of nitrided Ti6Al4V shows surface compound and diffusion layers. The compound layer comprising of TiN, Ti_2N, Ti_3Al, and $TiAl_2N$ phases is hard and brittle. The mechanical stability of this surface layer which is influenced by its porosity, cracks, and adhesion strength plays a key role in its performance [14,22,23]. Despite

using nitrogen with high purity for gas nitriding, the formation of oxide and oxynitride phases was found to be inevitable in high temperature nitriding [11,17,21]. Beneath the compound layer there is a homogeneous and relatively hard diffusion layer, which is caused by solid solution hardening. This layer is composed of mainly nitrogen enriched α grains, α-Ti(N), which play a key role in postponing the mechanical degradations such as wear and cavitation erosion [14,17,22,25]. However, Mitchell and Brotherton [26] reported that the fatigue limit of Ti6Al4V was reduced by gas nitriding. Bell et al. [23] attributed this reduction to variation of the core metal microstructure and formation of brittle α case on the surface. Very high concentration of interstitial elements such as oxygen and nitrogen in α case led to detrimental brittleness of this layer for the low cycle fatigue performance. This high concentration was considered as a defect in some cases and called High Interstitial Defect (HID) [1].

Ti6Al4V subjected to the solution-based and overaged treatments with bimodal microstructure is typically used for engine blade and disk applications [1,27]. The bimodal morphology is a combination of equiaxed and lamellar morphologies, two possible phase arrangements for α/β titanium alloys [1,2]. β-annealing followed by slow cooling results in a lamellar or basket-wave microstructure; whereas, equiaxial microstructure is formed by recrystallization [2]. Strength and ductility of α-β titanium alloys considerably depend on the ratio of α to β phases and their morphology. However, lamellar microstructure is generally known for its higher fracture toughness [1,2]. There is an ongoing debate about the fatigue behaviour of these titanium alloys [1,2,27]; indeed, the lamellar microstructure is more resistant to crack propagation, yet the equiaxial microstructure is more resistant to crack initiation. Typical duplex microstructure, which benefits from the advantages of both morphologies, is more common in aerospace industries. Although there is a debate in the literature regarding considering water droplet erosion as a fatigue problem [8,28], both involve cyclic loading conditions and are associated with surface cracking. Indeed, WDE was reported as having fatigue-like mechanism [3,8]. Hence, nitriding at temperatures above β-transus may be beneficial for the erosion application since it results in a lamellar microstructure of the substrate, which may decelerate crack growth. In this work, the influence of surface-nitrided layers and the variation of core material microstructure are considered to understand the resulting WDE performance. In addition, the effects of nitriding conditions including temperature, atmosphere and time are investigated on the erosion behaviour of nitrided samples.

2. Material and experimental procedures

2.1. Material

Ti6Al4V sheet with a thickness of 3 mm was received from Titanium industries Inc. It is an annealed Ti6Al4V (Grade 5) and its microstructure is composed of equiaxed α grains, retained β and small portion of the transformed β to co-orientated α plates. The α grains are significantly dominant constituent in this equiaxed microstructure, as shown in Fig. 1, and their mean size is 11 μm, which would be affected during the nitiding process.

These sheets were cut in the dimensions required for the water droplet erosion experiment which is 23 mm × 8 mm × 3 mm. Then, they were grinded using SiC papers to achieve a relatively smooth surface (average roughness of 0.06 μm). All specimens were cleaned using acetone and then rinsed in distilled water before the nitriding treatment.

2.2. Gas nitriding treatment

Gas nitriding was performed using a furnace with controlled atmosphere. The prepared specimens were mounted inside the reaction
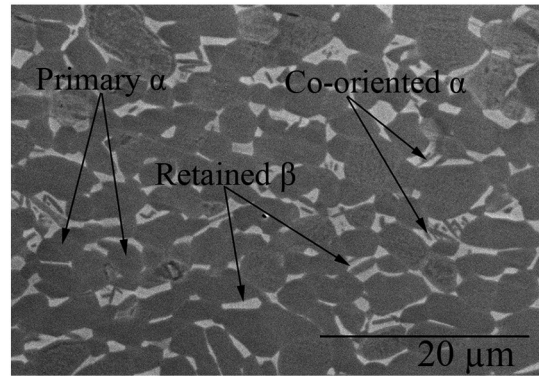

Fig. 1. SEM micrographs of as-received Ti6Al4V.

chamber and it was pumped down to 2×10^{-3} Pa. Different steps of the nitriding process are illustrated in Fig. 2.

The coupons nitrided with the above mentioned conditions are listed in Table 1. Further in the text, they will be referred to by their names that give clear indications of the different experimental conditions. In addition, as received Ti6Al4V and annealed Ti6Al4V at 1173 K and 1323 K for 5 h were considered as the reference coupons for erosion investigations. It is noteworthy that both nitriding and annealing were performed at temperatures higher (1323 K) and lower (1173 K) than the β transus temperature of Ti6Al4V, which is around 1273 K [29], in order to elucidate the effect of this transition on the nitriding process and the subsequent water droplet erosion performance.

2.3. Characterization of nitrided specimens

After the surface treatments, the phase constituents were investigated via X-ray diffraction (XRD) analysis. It was carried out using Cu-Kα radiation in a PANAnalytical X-ray diffractometer and to analyze XRD patterns, X'Pert HighScore Plus Rietveld analysis software [30] was used. In addition, Pearson's Crystal Database (PCD) [31] was used to identify the detected phases. The surface and cross section of nitrided specimens, prepared by standard metallographic techniques, were explored using optical microscope (OM), and scanning electron microscope (SEM, Hitachi S-3400 N). In order to reveal the microstructural features, cross section of nitrded coupons were etched using Kroll's Reagent etchant. Surface microhardness and microhardness profile of the specimens were measured using Vickers indenter at a load of 0.05 kgf (0.5 N) and 15 s dwell. The measurements were carried out on cross sections taken from the surface to the middle of the specimens. At each depth, at least five measurements were performed and their average was recorded.
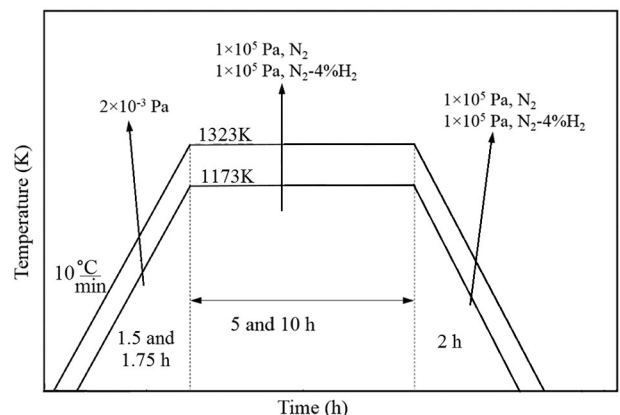

Fig. 2. Different steps of nitriding process.

Table 1
Nitriding conditions of Ti6Al4V.

Coupon number	Nitriding temperature (K)	Nitriding atmosphere	Nitriding time (h)	Coupon name
1	1173	100%N_2	5	1173 K-5 h
2	1173	100%N_2	10	1173 K-10 h
3	1323	100%N_2	5	1323 K-5 h
4	1323	100%N_2	10	1323 K-10 h
5	1173	96%N_2 + 4%H_2	5	H-1173 K-5 h

2.4. Water droplet erosion test

Water droplet erosion experiments were carried out using a rotating disk rig which was designed according to the ASTM G73 standard [32]. Details of this rig can be found in our previous publications [33,34]. In this study, droplet size of 464 μm (average) and impact speeds of 300 and 350 m/s were used for the erosion experiments. The chosen speeds are in the range of typical impact speeds for WDE of Ti6Al4V, which is 1.5 to 3 times of its damage threshold velocity [35]. They were performed in pre-set time intervals to construct erosion graphs. After each interval, the eroded samples were studied including microscopic examinations and weight loss measurements. This routine allows to detect the damage level of various layers by examining the erosion features over the damaged area using an optical microscope. By measuring the weight loss after each interval and knowing the density of target, the cumulative volume loss curves are plotted versus the cumulative erosion exposure. The incubation period (H_0) and maximum erosion rate (ER_{max}), the typical erosion indicators, could be obtained from these graphs according to ASTM G73 standard [32]. The vertical axis of the erosion graphs is the volume loss and the horizontal axis is the volume of impacting water and both are normalized by the area exposed to water droplets. Hence, a dimensionless maximum erosion rate could be reported. The area exposed to water droplets was measured from the optical micrographs of the eroded specimen recorded at the beginning of the maximum erosion rate stage.

The instantaneous erosion rate graphs, which were derived from the slope between two consecutive points on the volume loss curves, are also presented. Since the mechanical properties and microstructure of several layers in depth of Ti6Al4V were influenced by nitriding, the instantaneous erosion rate graphs are beneficial to track and associate the erosion behaviour and the damage mechanisms to the different layers.

In order to detect small changes in water erosion behaviour, it is important to always use an untreated Ti6Al4V sample as a reference coupon. This sample will counter balance the nitrided sample and will be used to gauge any improvement in water erosion performance. Thereby, the superiority graphs are presented minimize experimental errors, as detailed in our previous work [33]. During the erosion experiment the superiority of the nitrided coupon at each interval is defined according to Eq. (1). Then they are used for the superiority graphs. In these graphs positive value for the superiority means that the nitrided Ti6Al4V lost less material than the as-received one and vice versa. It is notable that the aforementioned superiority equation is invalid within the incubation of reference Ti6Al4V when its volume loss is zero.

$$\text{Superiority of nitrided Ti6Al4V}(\%)$$
$$= \frac{\text{Volume loss of Ti64} - \text{Volume loss of nitrided Ti64}}{\text{Volume loss of Ti64}} \quad (1)$$

To consider the total erosion performance of specimens, their cumulative erosion resistance as the reciprocal of cumulative material loss rate [36] will also be reported according to the following equation:

$$CER = \frac{1}{ER_F} = \frac{\text{Cumulative volume of impacted water}}{\text{Cumulative volume loss}} \quad (2)$$

where ER_F is the cumulative material loss (erosion) rate at the end of erosion tests, which is slope of the line connecting the origin to the last point of erosion graph. The experiments were stopped when the last stage of erosion, terminal steady state stage, was reached. In cases of 350 and 300 m/s impact speeds, the erosion tests were stopped after 15 and 60 min erosion, respectively. These time intervals correspond to 65 and 220 ml of water which impinged the specimens.

3. Results and discussion

3.1. Microstructural investigation

After nitriding, different colours were observed on the nitrided specimens. The coupons nitrided at 1173 K were mainly golden or purple/golden which indicates the formation of titanium nitride phases, as shown in Fig. 3. However, the samples nitrided at 1323 K for 5 and 10 h became dark grey/black and light grey, respectively. It indicates the formation of other phases in addition to titanium nitrides, which were explored using the X-ray diffraction technique. The XRD patterns of as-received Ti6Al4V and nitrided specimens are presented in Fig. 4. Strong α-Ti and weak β-Ti diffraction peaks were detected for the as-received Ti6Al4V. In the cases of nitrided specimens, α-Ti, TiN, TiNO, Ti_2N, $Ti_3AlO_{0.15}$ and TiO_2 peaks were revealed and there was no β-Ti peak. Ti6Al4V has considerable amount of aluminium and formation of relatively Al-rich phases such as Ti_2AlN and Ti_3Al was reported [22]. However, they were not detected in this work. Comparing the XRD spectrums of 1173 K-5 h and H-1173 K-5 h reveal that adding 4% hydrogen to the nitriding environment led to formation of more TiN compound on the surface, which have golden colour. In addition, α-Ti phase peaks display greater intensities for the coupons nitrided at higher temperatures. It is due to the higher diffusion of nitrogen in such specimens, stabilizing the α-Ti phase in the layers close to the surface. Despite the high purity of the nitrogen gas used for nitriding treatments, the oxide phases were observed for 1173 K-10 h, 1323 K-5 h, and 1323 K-10 h coupons. In case of the sample nitrided at 1173 K for 10 h, the main peaks belong to titanium nitride phases. However, the rutile and titanium oxynitride phases are also detected. Relatively higher level of oxide phases can be seen in the specimens nitrided at 1323 K. It seems that there was a higher chance for oxidation when nitriding was carried out at higher temperature, especially for longer time. This was also reported by others [11,17,21]. Titanium is very sensitive to oxygen particularly at temperature above 1073 K [29]; however, oxides formation is usually suppressed by low partial pressure of oxygen in nitriding treatment. Using higher temperature for nitriding results in the partial displacement of nitrogen by oxygen and the formation of titanium oxides within the surface layers. Rutile is an undesired phase for the applied treatment and would be detrimental for the mechanical properties and erosion performance. This may not be the case for titanium oxynitride phase, since Pohrelyuk et al. [37] highlighted its superior microhardness compared to that of titanium nitride. Generation of rutile
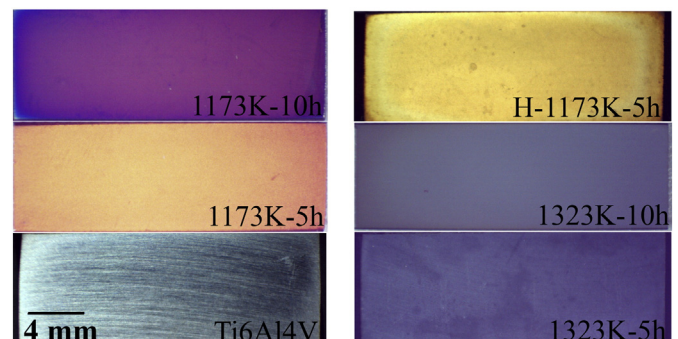

Fig. 3. Appearance of as-received Ti6Al4V and nitrided Ti6Al4V coupons.
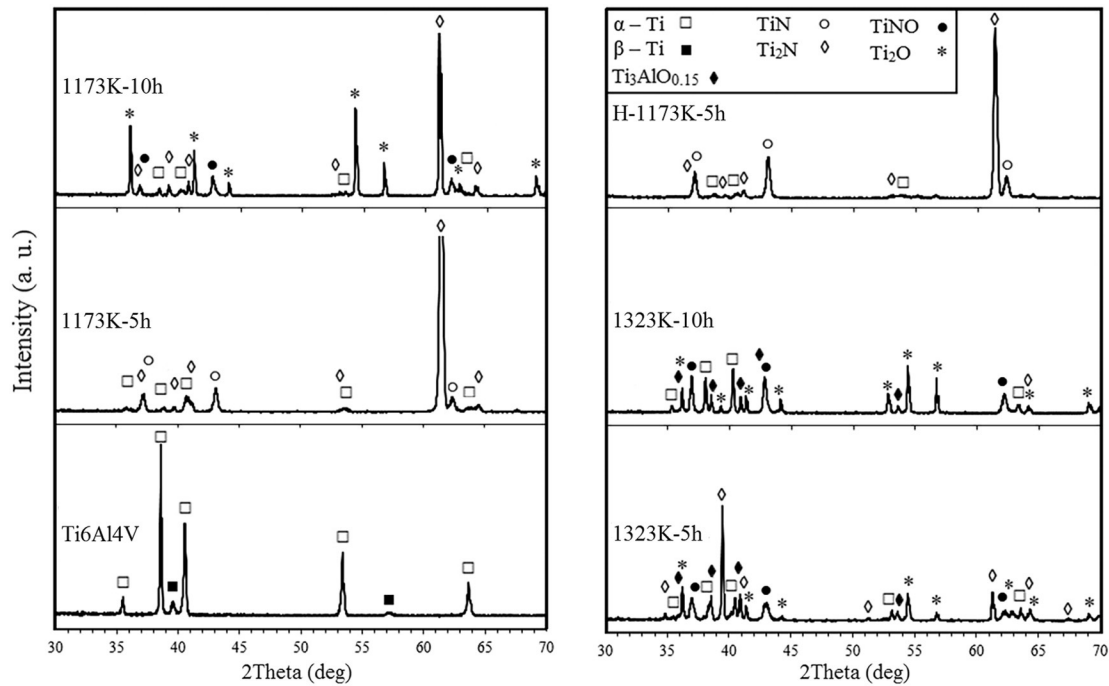
Fig. 4. XRD patterns of as-received Ti6Al4V and nitrided coupons.

and titanium oxynitride phases for the coupons nitrided at 1323 K influences their surface microhardness, as will be discussed in Section 3.2.

Fig. 5 shows the surface morphology of Ti6Al4V nitrided at 1173 and 1323 K temperatures for 5 h. These morphologies are affected by nitriding temperature, formed phases, and the growth type of outermost layer. At 1173 K, TiN compound with relatively fine and dense microstructure, composed of rounded agglomerates, were generated. However, TiO_2 compound with faceted structure predominantly form the outermost layer of nitrided Ti6Al4V at 1323 K. Titanium oxide is porous and relatively rough which is detrimental for erosion application.

Influence of nitriding temperature on the morphology and microstructure of nitrided layers are studied through the cross sectional micrographs using OM at low magnification and SEM at high magnification. Fig. 6 shows these micrographs for the coupon nitrided at 1173 K for 5 h. Four different areas, A, B, C, and D can be observed in the OM micrograph. Area A depicts the compounds layers, TiN and Ti_2N, and their microstructure at higher magnification can be seen in SEM micrograph, shown in Fig. 6-b. Relatively dense and thin TiN layer, 4 μm thickness, with crack-free interface is the outermost layer of the 1173 K-5 h

coupon. Within 5 to 15 μm from the surface an intermediate layer composed of two phases, Ti_2N and α-Ti(N), can be seen. Beneath the compound layers, nitrogen diffusion areas are shown. Detecting nitrogen with EDS detector was not possible because it is a very light element and its peaks overlap with titanium. Therefore, diffusion areas were determined by considering the microstructure variation. Nitrogen is an α stabilizer element and its diffusion pushes down β phase. Hence, diffusion layers are roughly identified based on the amount of α phase, which was measured using ImageJ software [38]. Region B has more than 90% α phase. Here, there are nitrogen enriched α grains and some retained β phase in their boundaries. Below this area, region C can be seen which is composed of more than 70% primary globular α grains and less than 30% lamellar colonies. Going further in depth, region D having less than 70% globular α grains can be seen. The amount of globular α grains in the core material, which was not influenced by diffusion of nitrogen, were found 65 ± 5%. Hence, region D is assumed as the part of coupon which was not influenced by nitrogen diffusion. However, the applied high temperature treatment changed the microstructure of this region where the average size of globular α grains
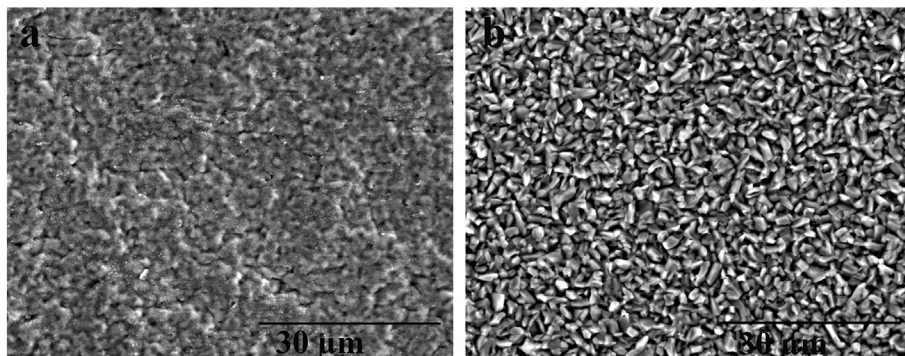

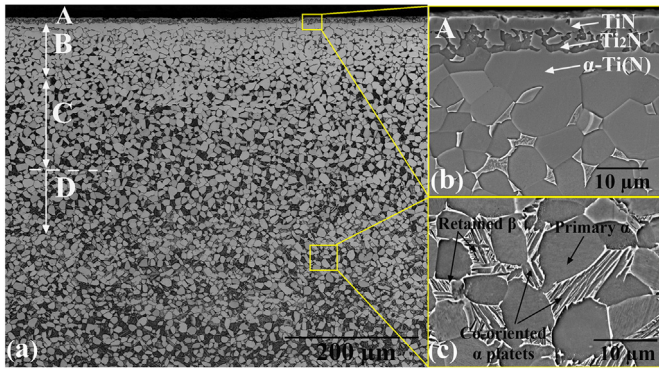**Fig. 5.** SEM micrographs of the surface of nitrided Ti6Al4V: (a) 1173 K-5 h, (b) 1323 K-5 h.

Fig. 6. (a) OM and (b,c) SEM cross sectional micrographs of Ti6Al4V nitrided at 1173 K for 5 h.

slightly increased. During the dwell time some α grains transformed to β phase and they became small colonies with basket-weave microstructure during the cooling. These colonies have lamellar configuration which is composed of co-oriented α lamellae separated by ribs of retained β, shown in Fig. 6-c. These lamellar colonies in the observed duplex microstructure may affect the cracking behaviour of nitrided coupons and subsequently their erosion performance.

Fig. 7 presents the cross sectional micrographs of Ti6Al4V nitrided at 1323 K for 5 h. In this micrograph also four distinct regions, A, B, C, and D are distinguished. Region A indicates the compounds layers, which are also displayed in the magnified SEM micrograph. Unlike nitriding at 1173 K, a relatively thick and porous TiO2 layer formed at 1323 K at the top surface having large number of pores and cracks at its interface. This porous layer is not mechanically stable and is significantly vulnerable. Beneath this layer, a thin and dense film can be seen which might be a mixture of TiNO and Ti_2N phases. The last part of A region is a mixture of $Ti_3AlO_{0.15}$ compound and saturated α phase. In the case of sample 1323 K-5 h, there is a notable difference for the morphology of areas affected by nitrogen diffusion. A β-free layer consisting of large α grains is highlighted as B region. The formation of this relatively thick and highly saturated layer with nitrogen and oxygen is explained by the fact that 1323 K is above β-transus temperature. Heating up to this temperature leads to the transformation of α to β phase. Nitrogen diffuses faster in bcc β phase due to its lower packing density compared to hcp α phase [2,10]. Its diffusion caused phase transformation from β to α in the dwelling stage of nitriding treatment [23]. In the cooling stage, the remained saturated β phase completely transforms to α phase at the area close to the surface and generates β-free region B. Below region B, a duplex microstructure including large and irregular α needles and large lamellar colonies can be seen as region C. Last region in this micrograph, D, is the part which was not affected by nitrogen diffusion. However, its microstructure was completely affected by the high temperature of applied treatment. Generation of such coarse and
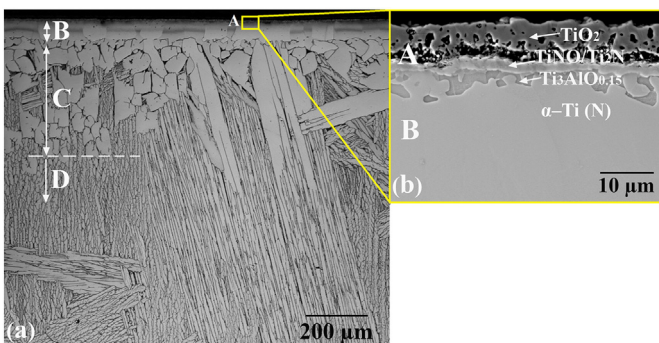
lamellar microstructure is due to the temperature of nitriding (above β-transus) followed by furnace cooling. At this temperature, the initial equiaxed α grains were dissolved and transformed to β phase. Then subsequent slow cooling from this temperature caused recrystallization and the generation of very large lamellar colonies consisting of co-oriented α plates separated by retained β. It is noteworthy that the large and irregular α needles observed in the closer areas to the surface, region C, are basically α plates which are enlarged in their preferred orientation due to the nitrogen diffusion.

The mechanism and kinetic of nitrogen diffusion at these two temperatures are different which lead to different phases, morphology and thickness of the surface layers. In the case of compounds layers, competition between the formation of nitride and oxide phases needs to be highlighted. Nitriding at high temperature caused the formation of porous titanium oxide layer which plays a key role in erosion damage initiation, as will be explained in Section 3.3.2. In the case of nitrogen diffusion areas not only their morphology, but also their mechanical properties (microhardness) were influenced by nitriding temperature. The nitrogen diffusion increases the hardness and plotting the microhardness profile over the cross section of nitrided coupons was conventionally used to reveal the thickness of diffusion layers. However, determining the depth of diffusion layers through the microstructure only is tricky because some of the observed differences can be results of particles segregation or phase transformations during the cooling. Hence, the microhardness profile measurements are explained in the following section.

3.2. Microhardness of nitrided specimens

Microhardness profiles in depth of the coupons nitrided at 1173 K are presented in Fig. 8. The first point in these graphs was measured on the surface and corresponds to hardness of layer A (compound layer). The second to fifth points in the hardness profile of sample 1173 K-5 h correspond to layer B (diffusion layer). In this layer notable increase in hardness compared to region D can be seen. Also, it is up to $675HV_{0.05}$ which is two times the hardness of as-received Ti6Al4V. In the deeper parts which correspond to layer C no increase in hardness is observed. The higher amount of α phase in layer C compared to layer D was attributed to the nitrogen diffusion as described in Section 3.1. Indeed, there is a slight diffusion which varies microstructure, but does not increase the hardness. Here, the highest surface hardness is observed for the sample nitrided at low temperature in the presences of hydrogen, H-1173 K-5 h. It is due to formation of a dense compound layer consisting of titanium nitride compounds in this condition. Lower surface hardness for the sample nitrided for the longer time can be seen in this figure. It is attributed to the formation of some oxide phases within the compound layer of 1173 K-10 h coupon. Nitriding time and the presence of H_2 do not affect the hardness of diffusion layer in the areas close to the surface (second point on the graphs); however, going deeper some variation can be seen. Thicker diffusion layer is detected for the sample nitrided for longer time, 1173 K-10 h. While hardness profile of 1173 K-5 h coupon reaches the hardness of core material at 90 μm distance from the surface, it reaches base hardness at 200 μm for 1173 K-10 h coupon. Furthermore, the presence of hydrogen in the nitriding environment does not influence the hardness of diffusion layer considerably. In spite of some fluctuations, similar trend can be seen for the hardness profile of 1173 K-5 h and H-1173 K-5 h coupons.

Fig. 9 shows the microhardness profiles over cross section of the coupons nitrided at 1323 K for 5 and 10 h. The different layers (A, B, C, and D) observed in the micrographs of the sample nitrided at 1323 K for 5 h and discussed in Section 3.1 are shown on this figure. Hardness of layer A or the compound layer is $988HV_{0.05}$ which was measured on the surface. The hardness within layer B was measured over the β-free layer, shown in Fig. 7. Its gradient indicates the change in the concentration of nitrogen in diffusion layer. Unlike 1173 K-5 h coupon, layers C and
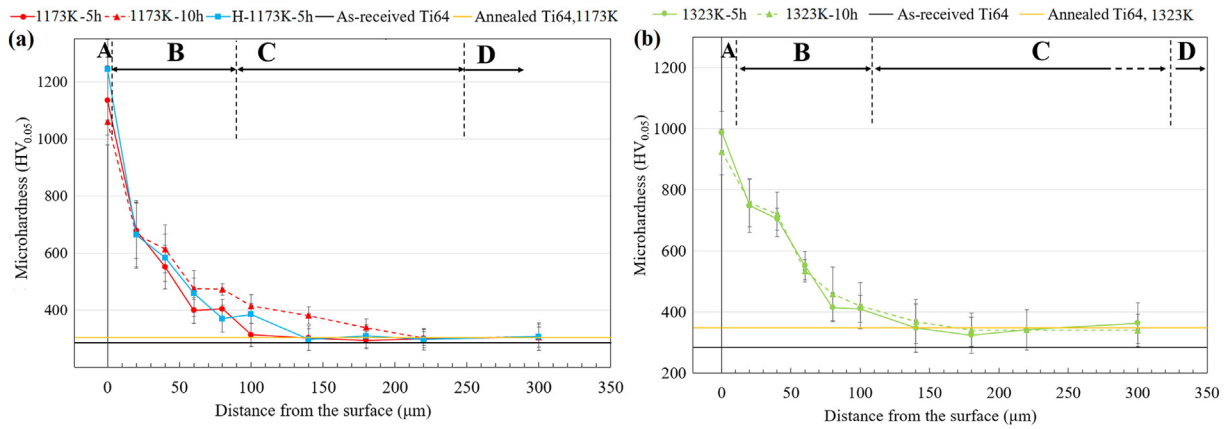

Fig. 7. (a) OM and (b) SEM cross sectional micrographs of Ti6Al4V nitrided at 1323 K for 5 h.

Fig. 8. Microhardness profiles of nitrided Ti6Al4V at: (a) 1173 K, (b) 1323 K.

D of sample nitrided at 1323 K is harder than as-received Ti6Al4V. In layer C, it is due to the formation of large α needles which was attributed to the slight diffusion of nitrogen at this temperature. It is noteworthy that the hardness of these layers is similar to the hardness of annealed Ti6Al4V at 1323 K for 5 h. Hence, the higher hardness cannot be easily correlated to nitrogen diffusion. Indeed, the lamellar-based morphology of these layers also contributes to the hardness increase. Furthermore, surface hardness of sample nitrided for 5 h is slightly higher than that of sample nitrided for 10 h. Similar hardness can be seen in depth of 1323 K-5 h and 1323 K-10 h samples (their diffusion layers). It seems that nitriding time does not notably affect the concentration of diffused nitrogen in layers B and C. This can be explained by the formation of thick compounds layers in high temperature nitriding which may impede further nitrogen diffusion at long nitriding treatments.

Comparing the hardness profiles in Figs. 8 and 9 show the significant influence of nitriding temperature on the hardness of nitrided coupons. Surface hardness of sample nitrided at 1173 K for 5 h is 1134HV$_{0.05}$ which is higher than that of sample nitrided at 1323 K for 5 h, 988HV$_{0.05}$. It is attributed to the nitrided compounds in the surface layer of 1173 K-5 h coupon which are harder than porous oxide compounds layer of 1323 K-5 h coupon. Nitridng temperature also affects the hardness of diffusion layers. Diffusion layer of sample nitrided at 1323 K (layer B) is approximately 100 HV harder than that of sample nitrided at 1173 K. It is explained by higher concentration of nitrogen and oxygen in the interstitial sites of titanium as a result of higher diffusion coefficient at this temperature. It is noteworthy that higher diffusion of nitrogen at 1323 K is mitigated notably by the formation of thick compound layer in the later stages of long nitriding treatments. Another difference between samples nitrided above and below β-transus temperature is the hardness of their core material. The hardness of 1173 K-5 h sample at 300 μm distance from the surface is 305HV$_{0.05}$, which is slightly higher (is considered within the error bars) than that of as-received Ti6Al4V (292HV$_{0.05}$). However, it is 364 for the 1323 K-5 h coupon, which is 74 HV higher than that of as-received Ti6Al4V.

3.3. Water droplet erosion

3.3.1. Water droplet erosion performance

Erosion behaviour of as-received, annealed and nitrided Ti6Al4V is presented in Fig. 9. Multi-layered nature of nitrided Ti6Al4V results in a non-uniform response to droplet impacts, unlike the non-treated Ti6Al4V. In our previous works erosion behaviour was found to be a function of the surface history, mechanical properties and local microstructure [6,33,34,39,40]. Figs. 6 and 7 display that local microstructures vary with depth for the nitrided specimens. Thereby, erosion damage at different layers is investigated using the instantaneous erosion rate graphs. All nitrided samples showed either negligible or a shorter incubation period compared to the as-received Ti6Al4V. The first two points

in the erosion graphs correspond mainly to the compounds layer performance and the next four mainly to the diffusion layers performance. Notable differences between the samples' erosion resistance are detected. These differences gradually decrease and eventually disappear and similar behaviour can be seen for all samples in the advanced stages of erosion, as shown in erosion rate graphs of Fig. 9.

3.3.1.1. Water droplet erosion performance at impact speeds of 350 m/s and 300 m/s. Fig. 9-a and b present the material loss and erosion rate graphs of the samples treated at 1173 K using impact speed of 350 m/s. Nitrided samples at this temperature for 5 and 10 h show more resistance compared to as-received Ti6Al4V. They demonstrate superior performance within the first six intervals. Their lower erosion rates in initial stages are attributed to the hard and dense nitrided layers which combat erosion damage. However, the compounds layer is relatively vulnerable and was partially damaged even in the first interval. The influence of nitrided layers particularly the diffusion layers to combat erosion damage can be verified by the lower erosion rates of the sample nitrided at 1173 K for 5 h compared to those of the Ti6Al4V annealed at the same condition. Although longer nitriding slightly increases the depth of diffusion layer, sample 1173 K-10 h shows more material loss compared to the sample nitrided for 5 h. It is attributed to its oxide compound layer which is mechanically unstable. Such layer is removed from larger area on the surface and leaves a cracked surface subjected to the next droplet impacts. This is detrimental for the performance of diffusion layers and is discussed further in Section 3.3.2. After six intervals all nitrided layers were removed and water droplets impacted the samples at depths that were not influenced by nitrogen diffusion, region D shown in Fig. 6. Therein, the difference of erosion behaviour is attributed to the different local microstructure. It seems that duplex microstructure, displayed in region D, is more resistant to erosion compared to the equiaxial microstructure of the as-received Ti6Al4V. This can be verified by lower erosion rates of annealed Ti6Al4V, which has duplex microstructure.

Fig. 9-c and d demonstrate the material loss and erosion rate graphs of the samples treated at 1323 K using impact speed of 350 m/s. There is no improvement in erosion resistance of Ti6Al4V nitrided at 1323 K. They show no incubation period, which is associated with complete detachment of the compounds layers in the first two intervals. These layers were removed from large area on the surface, which are demonstrated in Section 3.3.2. Despite the higher hardness of diffusion layer of nitrided samples at 1323 K, they do not show notable resistance to water droplet impacts. This can be realized from the high erosion rates of nitrided samples at initial intervals. Poor resistance of nitrided coupons at 1323 K can be explained by the early detachment of their porous compounds layers. Their detachment leaves a relatively rough surface, which is full of initiated cracks. These cracks can easily propagate with the induced stresses by further impacts and cause more material
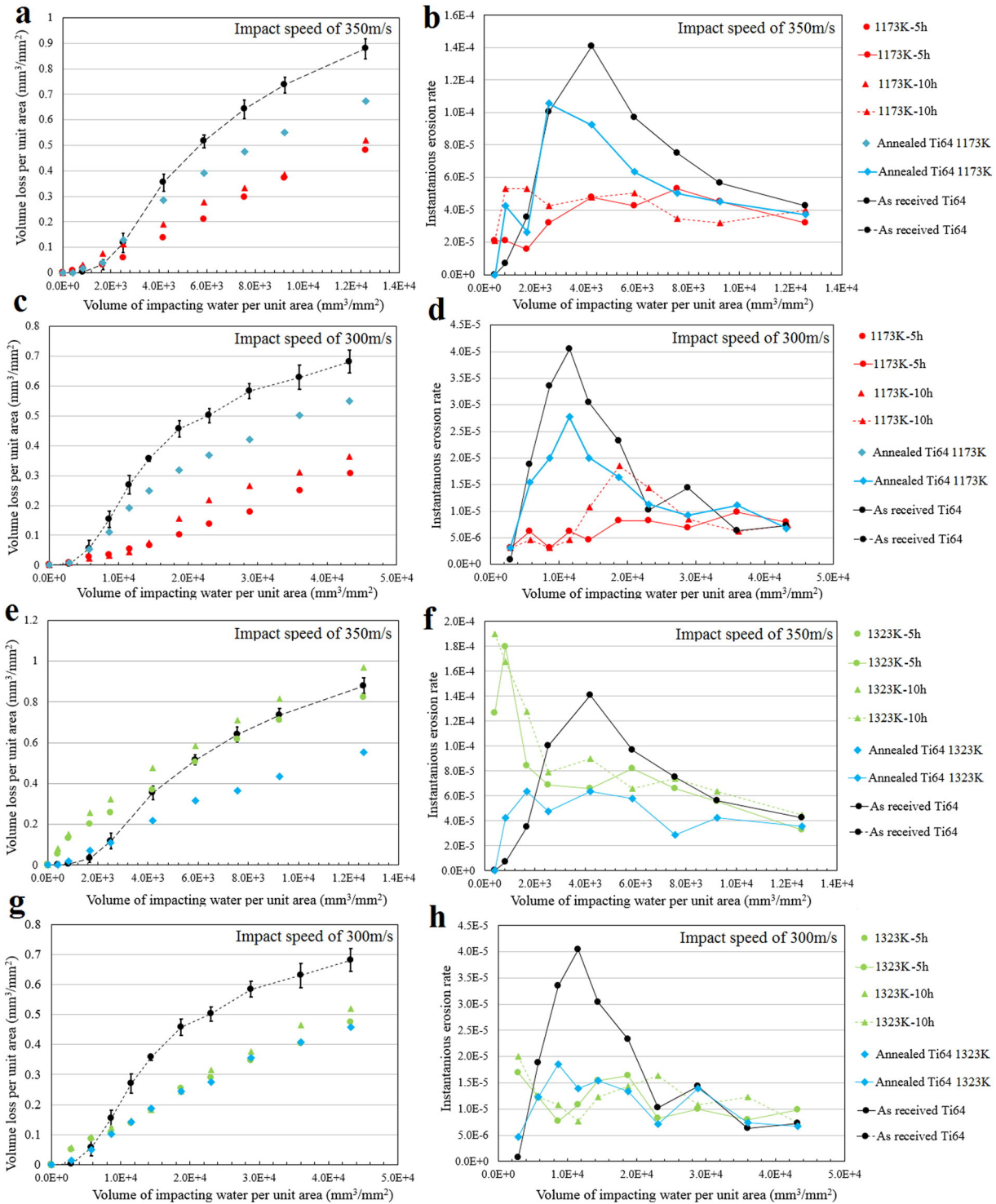
Fig. 9. WDE results of the samples treated at 1173 K and 1323 K using impact speed of 350 m/s and 300 m/s: (a,c,e,g) Normalized material loss versus volume of impinging water, (b,d,f,h) The instantaneous erosion rate at different intervals.

loss. This mechanism was documented and is explained in Section 3.3.2. Nitriding samples for longer time was not beneficial for erosion performance which can be attributed to the formation of thicker vulnerable compounds layers. In addition to the compound layer issues, very high concentration of interstitial elements (oxygen and nitrogen) in diffusion layer may lead to detrimental brittleness (HID defect) and contribute to the poor erosion resistance. Such defect in α case was highlighted as a potential reason for the lower fatigue limit of gas nitrided Ti6Al4V [23]. Superior erosion resistance of the annealed Ti6Al4V at 1323 K for

5 h compared to the nitrided sample at the same conditions indicates the detrimental role of porous and brittle nitrided layers to combat erosion damage. It is noteworthy that the sample annealed at 1323 K for 5 h, shows superior erosion resistance compared to the as-received Ti6Al4V. In water droplet erosion, the damage and material removal are governed by cracking. Hence, the crack growth rate which is function of local microstructure plays a key role to control material loss. The higher erosion resistance of β-annealed Ti6Al4V is attributed to the lower crack growth rate of its lamellar microstructure [2,27].

Fig. 9-e and f present the material loss and erosion rate graphs for the samples treated at 1173 K using impact speed of 300 m/s. The coupons nitrided at 1173 K for 5 and 10 h show considerably less erosion damage compared to the as-received and annealed Ti6Al4V. Nitrided layers in the initial stages, within the first six intervals, combat erosion damage and decelerate the material loss. In addition, the duplex microstructure of base material in nitrided coupons is slightly more erosion resistant compared to the equixial microstructure of the as-received Ti6Al4V. It can be verified by the lower erosion rates of annealed Ti6Al4V at 1173 K for 5 h, which is attributed to the cracking behaviour influenced by local microstructure. The longer nitriding treatment at this temperature is not beneficial for the erosion resistance and results in a slight increase in the erosion rate during the advanced stages. This could be attributed to the larger globular α grains observed in the sample nitrided for 10 h; these larger grains may facilitate the detachment of large fragments and increase the erosion rate.

Fig. 9-g and h present the material loss and erosion rate graphs for the samples treated at 1323 K using impact speed of 300 m/s. At this speed, nitrided Ti6Al4V show more erosion resistance compared to the as-received Ti6Al4V than the high speed experiments. The influence of impact speed on the erosion performance of sample nitrided at high temperature can be attributed to the different levels of stresses induced to the target, 1392 and 1148 MPa, by one droplet impact at 350 and 300 m/s speeds [33]. It seems that at higher speed there is sufficiently high exerted stresses to damage the micro-cracked surface left after the detachment of the compound layer. However, the imposed stresses and stress intensities at impact speed of 300 m/s would not be sufficient to propagate the cracks remained after the detachment of compounds layer. Hence, diffusion layer of the samples nitrided at 1323 K could combat droplet impacts and demonstrate lower erosion rates than as-received Ti6Al4V, as shown in Fig. 9-h.

3.3.1.2. Influence of nitriding atmosphere on the erosion performance. The influence of adding 4% H_2 to the nitriding environment on the erosion behaviour of the samples nitrided at 1173 K for 5 h was studied. Because the nitrided coupon at 1173 K for 5 h with pure nitrogen showed the best erosion resistance. Fig. 10-a shows the erosion results of 1173 K-5 h coupon, nitrided with N_2, and H-1173 K-5 h coupon, nitrided with N_2–4%H_2. There are small differences between the erosion graphs of these coupons, but the appearance of their eroded surface (within the first three intervals) showed notable difference. Hence, the superiority graphs are presented to study the performances of nitrided coupons with respect to their reference Ti6Al4V pair and detect small differences. Coupon H-1173 K-5 h displays more superiority than coupon 1173 K-5 h in the first two points, as shown in Fig. 10-b, where the compound

layer plays the most important role. This is due to the dense and crack free-compound layer consisting of titanium nitride compounds. These erosion results are consistent with the highest observed surface hardness for coupon H-1173 K-5 h, shown in Fig. 8-a. The erosion superiority of these samples at later stages of erosion are close. This is expected because of their similar microhardness and microstructures underneath the nitrided layers for both coupons.

3.3.1.3. Accumulated erosion resistance. Accumulated erosion resistances of the samples, derived using Eq. (2), are presented in Table 2. These numbers represent the influence of both nitrided layers and the local microstructure of core material on the erosion behaviour. In addition, the microhardness values of surface and diffusion layers (50 μm from the surface) are listed in Table 2. It is clear that nitriding at 1173 K for 5 h provides the best erosion performances. Coupons 1173 K-5 h and H-1173 K-5 h show the highest erosion resistance at 350 and 300 m/s impact speeds, respectively. For these coupons, the mechanical support of hard diffusion layer from the hard and dense compound layers results in their highest overall erosion resistance. Such mechanical support influences the failure mechanism of thin and hard compound layer. Lee et al. [41] highlighted that during the water droplet erosion of 12Cr steel coated by TiN films, the local depressions of ductile substrate is the main cause of hard film failure which leads to the circumferential cracking and fractures. In this case, a relatively hard diffusion layer beneath such hard and thin films diminish substrate deformations. Indeed, the diffusion layer may act as an intermediate layer and remove the large hardness mismatch within the interface between the hard film and ductile substrate. The beneficial role of diffusion layer to support top hard film, which leads to higher scratch or wear resistances, was reported in the literature [25,42,43]. In case of specimens 1323 K-5 h and 1323 K-10 h the impact speed considerably influences their erosion performances. For the aggressive erosion, carried out at higher impact speed, specimen 1323 K-5 h demonstrates similar erosion resistance to the as-received Ti6Al4V; however, it shows 44% higher erosion resistance at impact speed of 300 m/s. The influence of impact speed is more obvious in the case of specimen 1323 K-10 h. It showed 9% less erosion resistance than Ti6Al4V at impact speed of 350 m/s. However, reducing the impact speed to 300 m/s leads to a 31% higher resistance.

It is worthy to note that the annealed Ti6Al4V samples at both 1173 and 1323 K temperatures show higher cumulative erosion resistance compared to as-received Ti6Al4V. It is due to the different local microstructure of these samples. The slower crack propagation of lamellar colonies [27] is the main reason of such differences. It seems that lamellar microstructure is more resistant to erosion than duplex microstructure, and duplex microstructure is more resistant than equiaxial
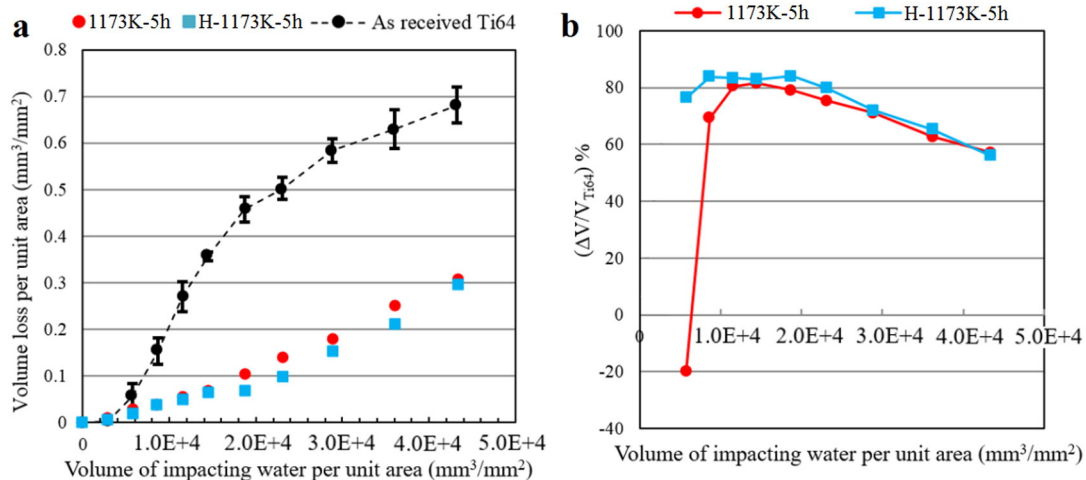

Fig. 10. Water droplet erosion results of nitrided Ti6Al4V at N_2 and N_2–4%H_2 environments using impact speed of 300 m/s: (a) Erosion graph, (b) Material loss superiority of nitrided Ti6Al4V compared to Ti6Al4V during the WDE test.

Table 2
Microhardness and erosion performance of as-received, annealed and nitrided Ti6Al4V.

Coupons	Surface microhardness	Microhardness of diffusion layer (50 μm from the surface)	Erosion resistance* at 350 m/s, CER/CER $_{Ti6Al4V}$	Erosion resistance* at 300 m/s, CER/CER $_{Ti6Al4V}$
1173 K-5 h	1134	510	1.83	2.24
1173 K-10 h	1060	570	1.69	1.87
1323 K-5 h	1035	641	1.07	1.44
1323 K-10 h	939	653	0.91	1.31
H1173 K-5 h	1243	551	1.74	2.34
As-received Ti6Al4V	292	292	1	1
Annealed Ti6Al4V at 1173 K	308	308	1.3	1.24
Annealed Ti6Al4V at 1323 K	348	348	1.59	1.49

* Calculated based on Eq. (2).

microstructure. This characteristic played a role mainly at the intermediate stages of erosion and ceased to have an influence at the advanced stages. Since the influence of nitrided or annealed Ti6Al4V microstructure on water droplet erosion performance is not the focus of this study, a future comprehensive study in this regard is recommended.

3.3.2. Characterization of erosion damage

Fig. 11 shows the plan-view of progressive damage during the erosion experiments. It is clear that the damage initiation is different for the samples nitrided for 5 h and as-received Ti6Al4V. These images indicate the high mechanical stability of compound layers and their resistance to droplet impacts for 1173 K-5 h and H-1173 K-5 h coupons, which were nitrided at low temperature. After 8 min, which corresponds to the second interval in Fig. 9-e and g, relatively large and scattered pits appeared on the surface of Ti6Al4V and led to detectable material loss. In this stage, 1173 K-5 h coupon lost its compound layer over the area impacted by water droplets. Also, a few small pits can be seen which indicate the local damage of diffusion layer. Further droplets caused the enlargement of these pits and their coalescence which led to the removal of diffusion layer. The erosion surfaces of 1173 K-5 h coupon and the as-received Ti6Al4V, Fig. 11-a and d, indicate that the damage level observed after 12 min for as-received Ti6Al4V is similar to the one observed after 50 min for 1173 K-5 h coupon.

The sample nitrided at 1323 K for 5 h was seen very vulnerable to the initial droplet impacts and its compounds layer was removed from a larger area on the surface, shown in Fig. 11-b. This detachment results in a notable peak at the beginning of the erosion rate graph, shown in Fig. 9-h. The erosion damage surfaces in the later intervals indicate the beneficial role of diffusion layer of 1323 K-5 h coupon to combat water droplet erosion. This layer decelerated pitting and formation of
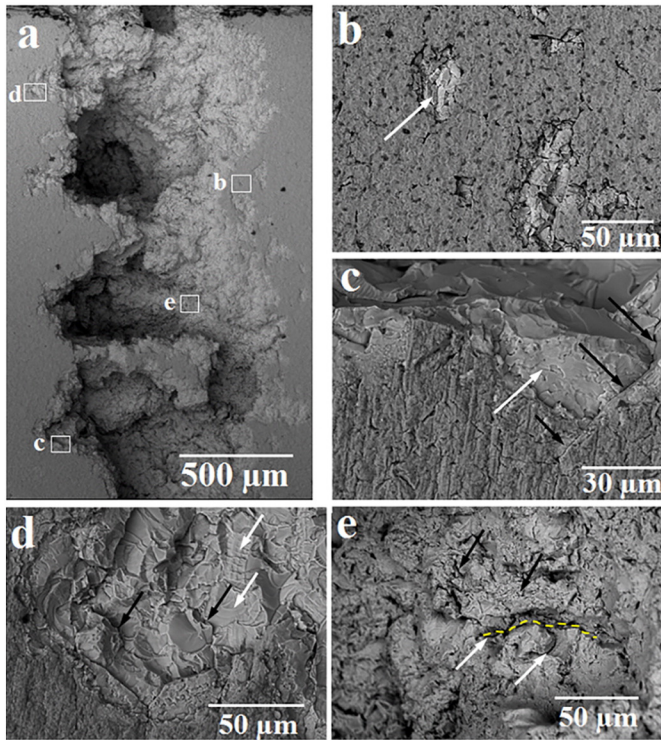
deep craters for this sample compared to as-received Ti6Al4V, shown in Fig. 11-b and d.

Losing the compound layer was also seen for the coupon nitrided at 1173 and in the presence of hydrogen. However, it is from smaller surface area compared to the other nitrided samples, shown in Fig. 11. It indicates the higher mechanical stability of the compounds layer formed in the reducing environment and confirms the superior performance of H-1173 K-5 h coupon compared to 1173 K-5 h coupon in the initial intervals, which was presented in Fig. 10-b.

Fig. 12 indicates the surface SEM micrographs of the sample nitrided at 1173 K for 5 h after it was eroded at the impact speed of 350 m/s. Deep erosion craters at the advanced stage can be seen in Fig. 12-a. It is clear that the erosion crater depth and width are not uniform along the area exposed to the droplet impacts. Severe damage and scattered deep pits can be seen over this area; however, some regions are not damaged significantly. The erosion damage initiation and its microstructural evolution can be seen in Fig. 12-b to e. The initial impacts cause the formation of crack networks and localized brittle fractures on the compound layer, shown in Fig. 12-b. The detachment of compounds layers results in the formation of relatively rough surface with a large number of nucleated cracks. These faceted cracks with a cleavage appearance are highlighted by arrows in Fig. 12-b,c, and d. Such cracked surface, which is basically the diffusion layer beneath the compounds layer, is prone to erosion upon further droplet impacts. According to the erosion results, diffusion layer plays an important role to combat water droplet erosion. This layer is supposed to impede cracking; however, numerous cracks which nucleated upon the compounds layer detachment, shown in Fig. 12-d, influence its performance. Indeed, the resistance of this layer to crack propagation controls its failure. Further impacts damage the diffusion layer by imposing local stresses leading to crack development, shown in Fig. 12-d. Water hammering and stress
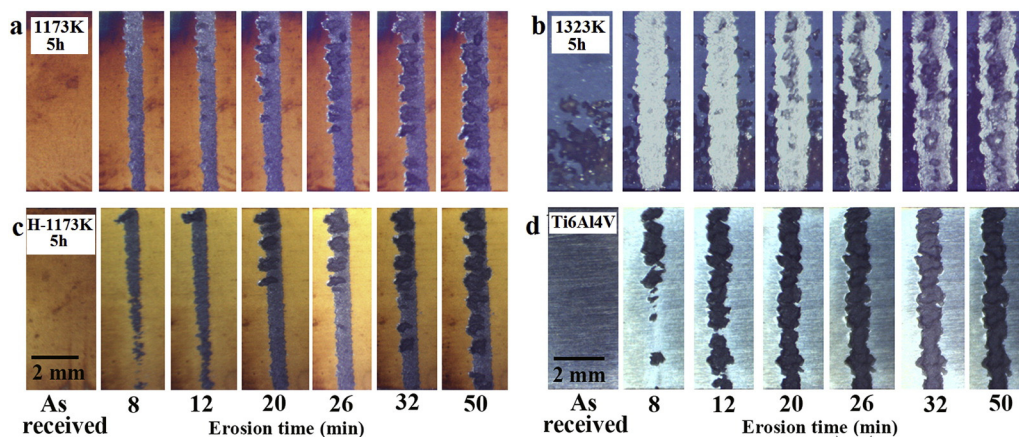
Fig. 11. Optical micrographs of erosion craters at different time intervals of the erosion experiments carried out at 300 m/s impact speed: (a) 1173 K-5 h, (b) 1323 K-5 h, (c) H-1173 K-5 h, (d) As-received Ti6Al4V.
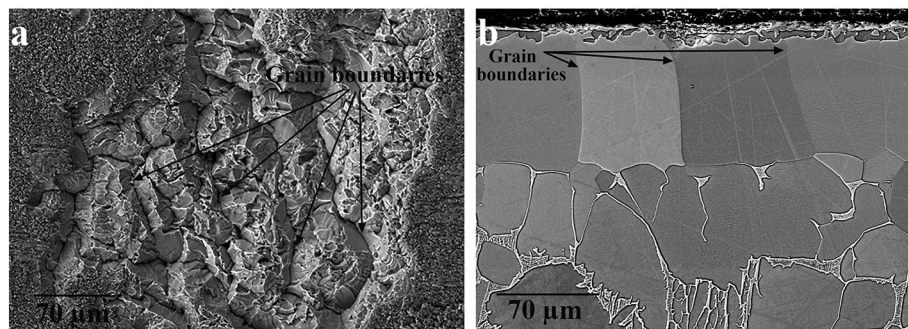
Fig. 12. Surface SEM micrographs of nitrided Ti6Al4V (1173 K-5 h) after erosion test: (a) erosion crater and deep pitting, (b) damage initiation on the compound layer, (c) top layers detachment at the edge of erosion crater, (d) erosion damage on diffusion layer, (e) eroded surface inside the erosion crater.

The mechanical stability of compounds layer has been considered as an influencing parameter on the erosion performance of diffusion layer. Surface intergranular crack, shown by black arrows in Fig. 12-c, indicates how the response of the compound layer affects the cracking behaviour of the diffusion layer. Here, a micro-crack initiated on the surface of brittle compound layer and the further droplet impacts made it to propagate into the diffusion layer. Hence, the hard diffusion layer cannot endure droplet impacts and would fracture faster leading to more material loss. In the case of sample nitriding at 1323 K, propagation of surface cracks into the diffusion layer and deteriorating the erosion resistance of this relatively brittle layer is the main reason for the poor erosion performance. The coupons eroded at 350 m/s suffered more from this type of cracking, since higher local stresses were induced at this speed. Fig. 13-a shows the slightly eroded surface of coupon 1323 K-5 h at this impact speed. Detachment of compound layer left numerous cracks on the surface of diffusion layer. Diffusion layer is hard and relatively brittle and nucleated cracks make it vulnerable upon further impacts. These cracks can be seen mainly along the boundaries of the large and enriched α grains, as shown by arrows in Fig. 13-a. These grains with similar sizes are demonstrated within α case of 1323 K-5 h coupon, as shown in Fig. 13-b. Such intergranular cracking into diffusion layer leads to its fast removal.

Fig. 14 presents the cross sections of eroded samples nitrided for 5 h at 1173 and 1323 K. Fig. 14-a shows the cross section of coupon 1173 K-5 h at the initial erosion stage. Several surface cracks, which are mainly developed due to water hammering, are highlighted by arrows. These cracks nucleate from either the compounds layer or the remaining surface after the detachment of the compound layer. Then, they propagate into the diffusion layer. No sub-surface crack, which is a known erosion damage feature in the early stages [40], could be detected over the cross section of eroded coupon 1173 K-5 h. It is due to the homogeneous microstructure of diffusion layer. A similar behaviour is observed for the sample nitrided at 1323 K, shown in Fig. 14-d, although it eroded faster than the sample nitrided at 1173 K. Here, the localized intergranular and transgranular cracks are indicated by black and white arrows in Fig. 14-a and d, which are consistent with the observed cracks on the surface.

Cross section of eroded coupons in the advanced stages are also presented. The depth of erosion crater is around 310 μm for coupon 1173 K-5 h, shown in Fig. 14-b, and 390 μm for coupon 1323 K-5 h, shown in Fig. 14-e. It is noteworthy that this depth varies along the erosion line, which was initially shown in Fig. 12-a. For both specimens, the material affected by nitrogen diffusion was removed completely. Here, the local microstructure of core material controls the progress of the damage. Coupon 1173 K-5 h, which was nitrided at 1173 K below β-transus temperature, shows the duplex microstructure of equiaxed α grains and small lamellar colonies. However, the Ti6Al4V nitrided at high temperature was treated above β-transus temperature, and during the cooling large colonies with co-oriented α lamellae within prior β grains were formed. This fully lamellar microstructure shows higher crack growth resistance compared to the equiaxal microstructure. It is due to the

waves propagation caused by repetitive droplet impacts are the main reasons for further cracking. The formation of striation marks on the eroded surface mainly over the facet of several grains, shown by white arrows in Fig. 12-d, indicates the cyclic growth of the cracks during erosion. It is worthy to note that the lateral jetting upon droplet impacts damages the surface asperities and initiates more cracks. More droplet impacts remove the nitrogen enriched α grains and the core material would be subjected to the droplet impacts. Once the nitrided layers are gone, the large and deep pits can be formed along the erosion crater. The scattering of these deep pits along the erosion line, shown in Fig. 12-a, could be attributed to the notable role of diffusion layer to combat erosion. When the diffusion layer was removed from a certain area, erosion damage quickly progressed in that area and deep pits were formed. Inhomogeneous loading inside the deep craters results in local damage and different types of cracking and fractures. The intergranular and transgranular cracks are highlighted by white and black arrows, respectively, in Fig. 12-e. Such cracks and fractures can be seen in the cross sectional micrographs discussed later in the text.

Fig. 13. (a) Surface SEM micrograph of slightly eroded 1323 K-5 h sample, (b) cross section of 1323 K-5 h sample (non-eroded) showing diffusion layer.
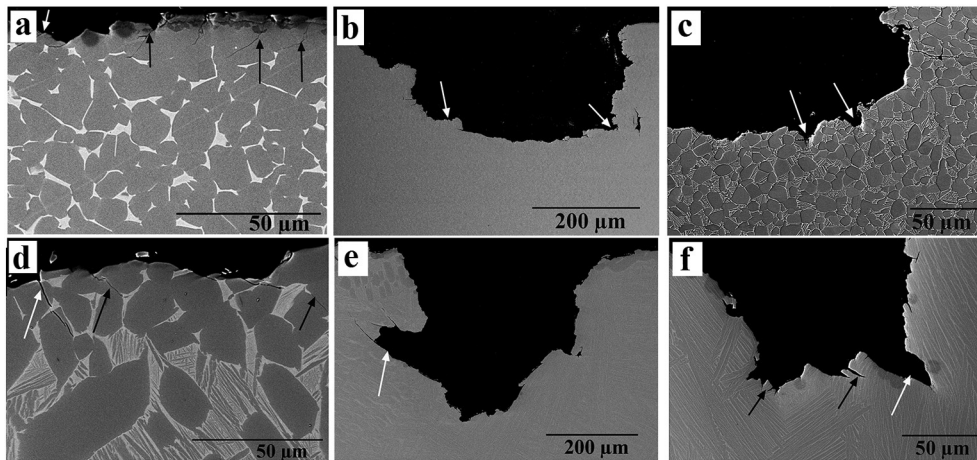
Fig. 14. Cross sectional SEM micrographs of eroded (a,b,c) 1173 K-5 h coupon and (d,e,f) 1323 K-5 h coupon which show: (a and d) Erosion damage of nitrided layers, (b and e) Main erosion crater at low magnifications, (c and f) Cracks propagation and water penetration.

larger degree of cracks deflection, bifurcation and secondary cracks formation, which were reported as the toughening mechanism in lamellar microstructures [2,27,44]. The slower crack growth of lamellar microstructures leads to the superior erosion performance of annealed Ti6Al4V compared to the *as*-received one.

In addition to the water hammering and propagating stress waves into the target, water penetration (caused by hydrodynamic pressures) is an important reason for crack growth and fracture. Water hammering and initial fractures firstly cause the formations of relatively small cavities. Further droplets and subsequent water penetration dig the bottom of the small cavities and generate either deep and elliptical or narrow and undercutting pits. Fig. 14-c shows the formation of deep and elliptical pits at the bottom of erosion crater within duplex microstructure. Fig. 14-f demonstrates the narrow and undercutting pits within the lamellar microstructure. The observed erosion features along with the instantaneous erosion rate graphs reveal two different erosion mechanisms for these microstructures. Indeed, the small grain size of duplex microstructure results in the acceleration of cracks coalescence and subsequent material loss. Hence, fast and frequent detachment of small fragments is the dominant mechanism for the erosion of bimodal microstructure. In contrast, the cracks deflection and bifurcation decelerate the cracks propagation within the lamellar microstructure. Thereby, slow and infrequent detachment of relatively large portions could be mentioned as the dominant material loss mechanism for this microstructure.

3.4. Conclusions

Water droplet erosion performance of nitrided Ti6Al4V at different conditions were studied. Different erosion indicators were considered to track the erosion damage during the whole test. In addition, the microstructural investigation on the surface and cross section of eroded coupons revealed the erosion mechanisms. The following conclusions can be drawn:

1. Gas nitriding generated a very hard and brittle compounds layer and a relatively hard and homogeneous diffusion layer in Ti6Al4V. Nitriding conditions particularly the temperature altered the resulting layers as well as the core material microstructure which influenced the cracking behaviour and subsequently the erosion performance.

2. The Ti6Al4V nitrided at 1173 K showed the best erosion resistance, which is measured by their corresponding cumulative material loss and is 70% to 125% higher than the as-received Ti6Al4V and 40% to 80% higher than annealed Ti6Al4V at 1173 K. Hard and dense compounds layer which is mechanically supported by the homogeneous diffusion layer led to the superior erosion performance of these

nitrided coupons. For WDE applications, temperatures below β transus (e.g. 1173 K) and 5 h would be the best nitriding conditions. Also, to avoid undesired microstructure variations and make nitriding more practical treatment to combat WDE of turbine blades, localized heating source could be used.

3. Erosion performance of Ti6Al4V nitrided at 1323 K was notably sensitive to the impact velocity. At 350 m/s, the nitrided coupon showed either a worse or similar performance to the as-received Ti6Al4V. However, they displayed up to 44% higher resistance than the as-received Ti6Al4V when the impact speed was decreased to 300 m/s. This superior performance was attributed to the relatively hard diffusion layer and the lamellar microstructure of core material.

4. Nitriding in the presence of hydrogen enhanced the hardness of compounds layer and led to its higher mechanical stability. Ti6Al4V nitrided in the presence of hydrogen displayed slightly higher resistance during the initial stages of water droplet erosion.

References

[1] R. Wanhill, S. Barter, Fatigue of Beta Processed and Beta Heat-Treated Titanium Alloys, Springer Briefs in Applied Sciences and Technology, 2011.
[2] C. Leyens, M. Peters, Titanium and Titanium Alloys, Weinheim, WILEY-VCH, 2003.
[3] F.J. Heymann, Liquid Impingement Erosion, ASM Hanbbook, Wear, ASM International, 1992.
[4] R.K. Bhargava, C. Meher-Homji, M.A. Chaker, M. Bianchi, F. Melino, A. Peretto, S. Ingistov, Gas turbine fogging technology: a state-of-the-art review-part II: overspray fogging-analytical and experimental aspects, Trans. ASME. Eng. Gas Turbines Power 129 (2007) 454–460.
[5] L. Huang, J. Folkes, P. Kinnell, P.H. Shipway, Mechanisms of damage initiation in a titanium alloy subjected to water droplet impact during ultra-high pressure plain waterjet erosion, J. Eng. Gas Turbines Power 212 (2012) 1906–1915.
[6] D. Ma, A. Mostafa, D. Kevorkov, P. Jedrzejowski, M. Pugh, M. Medraj, Water impingement erosion of deep-rolled Ti64, Metals (2015) 1462–1486.
[7] N. Kamkar Zahmatkesh, Water Droplet Erosion Mechanisms of Ti-6Al-4 VPhD Thesis at École de Technologie Supérieure, 2014.
[8] G.S. Springer, Liquid Droplet Erosion, John Wiley & Sons, New York, 1976.
[9] N.L. Hancox, J.H. Brunton, The erosion of solids by the repeated impact of liquid drops, Philos. Trans. R. Soc. Lond. A Math. Phys. Sci. 260 (1966) 121–139.
[10] H. Dong, Surface Engineering of Light Alloys: Aluminium, Magnesium and Titanium Alloys, Elsevier, 2010.

[11] M. Nakai, M. Niinomi, T. Akahori, N. Ohtsu, H. Nishimura, H. Toda, H. Fukui, M. Ogawa, Surface hardening of biomedical Ti–29Nb–13Ta–4.6 zr and Ti–6Al–4 V ELI by gas nitriding, Mater. Sci. Eng. A 486 (2008) 193–201.

[12] C. Gerdes, A. Karimi, H.W. Bieler, Water droplet erosion and microstructure of laser-nitrided ti-6Al-4 V, Wear 186–187 (1995) 368–374.

[13] P. Lammel, L.D. Rafailovic, M. Kolb, K. Pohl, A.H. Whitehead, G. Grundmeier, B. Gollas, Analysis of rain erosion resistance of electroplated nickel-tungsten alloy coatings, Surf. Coat. Technol. 206 (2012) 2545–2551.

[14] A. Zhecheva, W. Sha, S. Malinov, A. Long, Enhancing the microstructure and properties of titanium alloys through nitriding and other surface engineering methods, Surf. Coat. Technol. 200 (2005) 2192–2207.

[15] H. Shibata, K. Tokaji, T. Ogawa, C. Hori, The effect of gas nitriding on fatigue behaviour in titanium alloys, Int. J. Fatigue 16 (1994) 370–376.

[16] K. Zhou, H. Herman, Cavitation erosion of titanium and Ti-6 A1-4 V: Effects of nitriding, Wear 80 (1982) 101–113.

[17] H. Li, Z. Cui, Z. Li, S. Zhu, X. Yang, Effect of gas nitriding treatment on cavitation erosion behavior of commercially pure Ti and Ti − 6Al − 4 V alloy, Surf. Coat. Technol. 221 (2013) 29–36.

[18] I. Mitelea, E. Dimian, I. Bordeaşu, C. Crăciunescu, Ultrasonic cavitation erosion of gas nitrided Ti–6Al–4 V alloys, Ultrason. Sonochem. 21 (2014) 1544–1548.

[19] H.C. Man, Z.D. Cui, T.M. Yue, F.T. Cheng, Cavitation erosion behavior of laser gas nitrided ti and Ti6Al4V alloy, Mater. Sci. Eng. A 355 (2003) 167–173.

[20] M. Shiomi, E.C. Santos, M. Morita, K. Osakada, M. Takahashi, Laser gas nitriding of pure titanium using CW and pulsed nd:YAG lasers, Surf. Coat. Technol. 201 (2006) 1635–1642.

[21] A. Zhecheva, S. Malinov, W. Sha, Titanium alloys after surface gas nitriding, Surf. Coat. Technol. 201 (2006) 2467–2474.

[22] H. Spies, Surface engineering of aluminium and titanium alloys: an overview, Surf. Eng. 26 (2010) 126–134.

[23] T. Bell, H.W. Bergmann, J. Lanagan, P.H. Morton, A.M. Staines, Surface engineering of titanium with nitrogen, Surf. Eng. 2 (1986) 133–143.

[24] S. Malinov, A. Zhecheva, W. Sha, Relation between the microstructure and properties of commercial titanium alloys and the parameters of gas nitriding, Met. Sci. Heat Treat. 46 (2004) 286–293.

[25] M.S. Mahdipoor, F. Mahboubi, S. Ahangarani, M. Raoufi, H. Elmkhah, The influence of plasma nitriding pre-treatment on tribological properties of TiN coatings deposited by PACVD, J. Mater. Eng. Perform. 21 (2012) 958–964.

[26] E. Mitchell, P.J. Brotherton, Surface treatments and lubricants for improving press-forming properties of titanium and its alloys, J. Inst. Met. 93 (1965) 278–279.

[27] R.K. Nalla, B.L. Boyce, J.P. Campbell, J.O. Peters, R.O. Ritchie, Influence of microstructure on high-cycle fatigue of Ti-6Al-4 V: Bimodal vs. lamellar structures, Metall. Mater. Trans. A 33 (2002) 899–918.

[28] A. Thiruvengadam, S.L. Rudy, M. Gunasekaran, Experimental and analytical investigations on liquid impact erosion, Characterization and Determination of Erosion Resistance, ASTM STP 474 1970, pp. 249–287.

[29] A. Zhecheva, S. Malinov, W. Sha, Surface gas nitriding of ti-6Al-4 V and ti-6Al-2Sn-4Zr-2Mo-0.08 si alloys, Z. Metallkd. 94 (2003) 19–24.

[30] PANalytical, Ver2.2b (2.2.2), PANalytical, Almelo, The Netherlands, 2006.

[31] H. Putz, K. Brandenburg, Pearson's Crystal Data, Crystal Structure Database for Inorganic Compounds, CD-ROM Software Version 1, 3, 2009.

[32] ASTM G73–10, Standard Test Method for Liquid Impingement Erosion Using Rotating Apparatus, ASTM International, West Conshohocken, 2010.

[33] M.S. Mahdipoor, H.S. Kirols, D. Kevorkov, P. Jedrzejowski, M. Medraj, Influence of impact speed on water droplet erosion of TiAl compared with Ti6Al4V, Sci. Rep. 5 (2015).

[34] H.S. Kirols, D. Kevorkov, A. Uihlein, M. Medraj, The effect of initial surface roughness on water droplet erosion behaviour, Wear 342 (2015) 198–209.

[35] F.J. Heymann, Survey of clues to the relationship between erosion rate and impact conditions, Second Meersburg Conference on Rain Erosion and Allied Phenomena, Bondensee, Fedreal German Republic 1967, pp. 683–760.

[36] M. Ahmad, M. Casey, N. Sürken, Experimental assessment of droplet impact erosion resistance of steam turbine blade materials, Wear 267 (2009) 1605–1618.

[37] I.M. Pohrelyuk, V.M. Fedirko, O.V. Tkachuk, Effect of the rarefaction of an oxygen-containing medium on the formation of titanium oxynitrides, Mater. Sci. 44 (2008) 64–69.

[38] M.D. Abràmoff, P.J. Magalhães, S.J. Ram, Image processing with ImageJ, Biophoton. Int. 11 (2004) 36–42.

[39] M.S. Mahdipoor, F. Tarasi, C. Moreau, A. Dolatabadi, M. Medraj, HVOF sprayed coatings of nano-agglomerated tungsten-carbide/cobalt powders for water droplet erosion application, Wear 330 (2015) 338–347.

[40] M.S. Mahdipoor, D. Kevorkov, P. Jedrzejowski, M. Medraj, Water droplet erosion mechanism of nearly fully-lamellar gamma TiAl alloy, Mater. Des. 89 (2016) 1095–1106.

[41] W. Lee, W.W. Kim, C.K. Rhee, W.J. Lee, Liquid impact erosion mechanism and theoretical impact stress analysis in TiN-coated steam turbine blade materials, Metall. Mater. Trans. A 30 (1999) 961–968.

[42] Y. He, I. Apachitei, J. Zhou, T. Walstock, J. Duszczyk, Effect of prior plasma nitriding applied to a hot-work tool steel on the scratch-resistant properties of PACVD TiBN and TiCN coatings, Surf. Coat. Technol. 201 (2006) 2534–2539.

[43] M. Raoufi, S. Mirdamadi, F. Mahboubi, S. Ahangarani, M.S. Mahdipoor, H. Elmkhah, Effect of active screen plasma nitriding pretreatment on wear behavior of TiN coating deposited by PACVD technique, Appl. Surf. Sci. 258 (2012) 7820–7825.

[44] F. Appel, J. Paul, M. Oehring, Gamma Titanium Aluminide Alloys: Science and Technology, John Wiley & Sons, 2011.